Journal of Corrosion and Materials
www.corromat.com

J. Corros. Mater. (2022) 1(1), 28–41.

An Oxygen-Tolerant Lamellar Spacing Window for Eutectic Al–Cu Anodes in Aqueous Aluminum–Manganese Batteries

Evan J. Reed[1,*], Ethan Jay Carter[2]

[1] *Department of Materials Science and Engineering, Stanford University, Stanford, CA 94305-4034, USA*
[2] *College of Engineering, University of Michigan, G.G. Brown Laboratory, 2350 Hayward Street, Ann Arbor, MI 48109, USA*

[*]Corresponding author: evanreed@stanford.edu
[2] ethanjay.carter099@gmail.com

(Received: 11 February 2022. Received in revised form: 9 May 2022. Accepted: 25 May 2022. Published online: 30 June 2022.)

Abstract

Rechargeable aluminum batteries in aqueous electrolytes have promise due to safety, cost, and abundance considerations; however, the metal-anode negative electrodes suffer from oxide/hydroxide films, hydrogen evolution, dissolved oxygen corrosion, and non-uniform stripping/plating morphologies. The central design challenge is whether the lamellar period of the eutectic Al–Cu alloy can be engineered to meet the oxygen-normalized criterion of both symmetric-cell reversibility and full-cell energy utilization with a hydrated aluminum manganese oxide cathode. The set of electrodes under investigation includes eutectic $Al_{82}Cu_{18}$ lamellar periods of 180, 280, 420, 650, and 1100 nm, as well as pure Al and monolithic Al_2Cu electrodes; all are tested in aqueous 2 M $Al(OTF)_3$ electrolyte at dissolved oxygen concentrations of 0.13, 1.5, 5.0, and 13.6 mg L^{-1}. It is found that the choice of optimal structure cannot be reduced to maximizing the Al/Al_2Cu interfacial density. The 180 nm electrode shows maximum interfacial density but higher sensitivity to oxygen-facilitated cathodic side reactions, while 650 and 1100 nm electrodes have problems related to increased Al diffusion distances and passivation-induced polarization. The 280 nm lamellar period results in the most effective performance: the overpotential in low-oxygen concentration environment decreases from 53 to 38 mV in comparison with the 420 nm electrode reference case, the charge transfer resistance reduces from 160 to 112 Ω, stable stripping/plating increases from 2000 to 3000 h, and a full-cell based on $Al_xMnO_2 \cdot nH_2O$ cathode delivers a capacity of 492 mAh g^{-1} at 0.1 A g^{-1}, 215 mAh g^{-1} at 5 A g^{-1}, energy density of 706 Wh kg^{-1}, and maintains 88% after 600 cycles. The key result is that the lamellar Al–Cu alloy should be engineered into a specific range of oxygen tolerance between 240 and 330 nm.

Keywords: aqueous aluminum battery; aluminum anode; eutectic Al–Cu; lamellar spacing; dissolved oxygen; galvanic accessibility; impedance; manganese oxide cathode.

1. Introduction

The chemistry for large-scale electrical storage needs to provide a combination of safety, natural abundance, ease of synthesis, and reliability of function in realistic environments. Aluminum-based rechargeable batteries are especially interesting here due to the abundance, recyclability, low price, and three-electron redox properties of aluminum. Al metal has a theoretically possible specific energy of 2981 mAh g^{-1} and volumetric capacity of about 8056 mAh cm^{-3}, putting aluminum among the best metal candidates in terms of capacity. These figures, however, do not immediately give aqueous rechargeable battery performance. In wet electrolytes, aluminum creates a protective oxide and hydroxide film, is subject to self-corrosion, and competes with hydrogen evolution. The net result is a negative electrode that is an electrochemical reagent, a corrosion substrate, and a morphological issue [1–4, 6, 7].

The problem with an aqueous aluminum battery anode is of a very different character compared to the common task of finding a host material. In most lithium-ion electrodes, the activity is ensured by a reversible intercalation or alloying in a solid phase, while interphase engineering maintains such reaction over multiple cycles [4, 5]. Metal aluminum in aqueous media fails at the metal-water interface before its theoretical capacity can be utilized. The protective film stops the diffusion of Al^{3+} ions, a localized rupture in the film concentrates the electric field, cathodic sites provide a locus of water reduction and oxygen reduction, and a selective redeposition of the deposited metal may happen. As corrosion science has always indicated, a local pH rise, pit chemistry, intermetallic particles, and oxide healing define the fate of the aluminum surface in aqueous media [8–12]. A functional rechargeable anode must regulate both charge transfer and corrosion morphology.

The nonaqueous aluminum-ion batteries and chloroaluminate ionic liquids have demonstrated that reversible aluminum electrochemistry is possible, especially in cases where electrolyte chemistry allows for Al complexation and stripping/plating without a dominant water reduction path [13–15]. Such batteries still do not solve the need for cost-effective aqueous electrolytes. An aqueous medium increases the significance of self-corrosion, passivation, gas evolution, and oxygen leakage in addition to being non-flammable and easier to process. Recent reviews of aqueous aluminum-ion and aluminum metal batteries recognize the anode as one of the critical obstacles for long cycle life, along with cathode stability and solvation control [16–22]. In this sense, an anode is not just another Al foil, but a microstructured electrode whose phase geometry must be designed for the chemical environment.

The progress in positive-electrode development raises the anode question to even higher prominence. Some of the early aqueous aluminum-ion research has demonstrated reversible aluminum storage in anatase TiO_2 nanotubes, Prussian blue

analogues, copper hexacyanoferrate, and cation-deficient titanium oxides [23–26]. Especially important for us are hydrated or electrochemically activated Mn oxides since $Al_xMnO_2 \cdot nH_2O$ can store high capacity in aqueous Al salt electrolyte while accommodating charge compensation through Al species and water [27, 28]. However, such cathode can exploit its available potential window only if the anode does not spend it all with polarization and hysteresis. In this sense, a smaller anode overpotential is not just an anode measure; it defines how much cathode capacity is available in aqueous $Al/Al_xMnO_2 \cdot nH_2O$ batteries.

Eutectic Al-Cu alloying offers a microstructure for the control of the anode interface. At the $Al_{82}Cu_{18}$ composition, the alloy solidifies into alternating α-Al and Al_2Cu lamellae. Electroactive aluminum is supplied by Al lamellae, while more noble and conductive Al_2Cu phase serves as a repeated network of electron collection and current redistribution nodes. Ran et al. showed that lamellar Al-Cu structures increase aluminum electrochemical reversibility, reduce the risk of dendrites, and enable high-energy aqueous $Al/Al_xMnO_2 \cdot nH_2O$ cells in 2 M $Al(OTF)_3$ electrolyte [7]. In their experiment, the reference lamellar alloy had Al and Al_2Cu lamellae of approximately 150 and 270 nm thickness, respectively, resulting in the period of nearly 420 nm. The open question is whether this period is optimal for the electrolyte with varying amounts of dissolved oxygen.

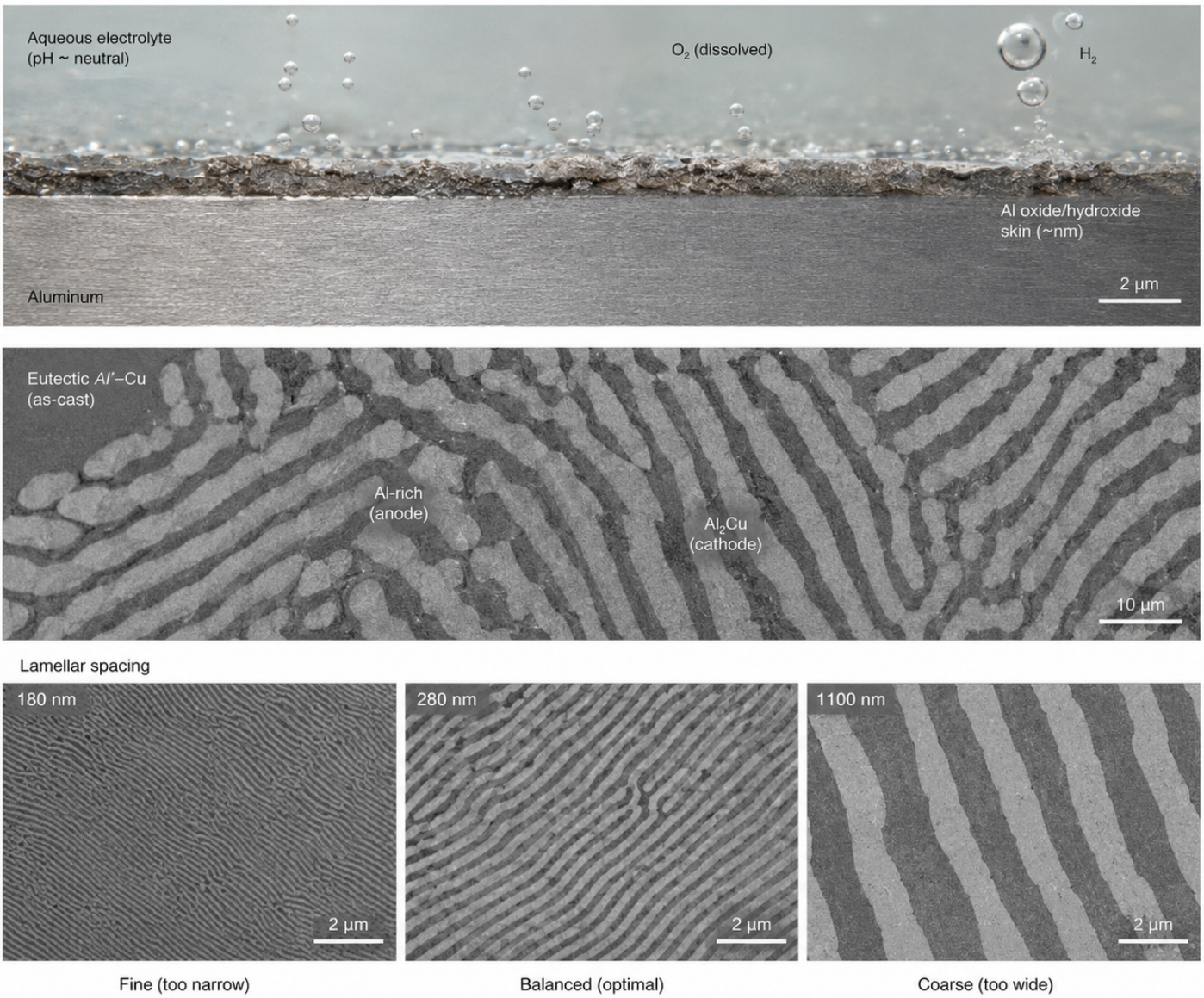

Figure 1: Surface instability and lamellar spacing states.

The open length scale question is therefore the selection of an appropriate period that will provide an improvement in reversibility without increasing oxygen-induced side reactions. Smaller lamellar spacing will provide a greater number of Al/Al_2Cu interfaces and the shorter path from an active Al site to a conductive intermetallic guide. This should help to increase uniformity of plating/stripping and lower charge-transfer resistance. At the same time, a finer period means a larger number of cathodic intermetallic sites, which could enhance oxygen and water reduction in a not perfectly deaerated electrolyte. A coarse spacing decreases the cathodic intermetallic area but exposes wider aluminum channels to passivation and selective dissolution. The design principle cannot be "the finer the lamellae – the better." It has to find a spacing that balances access length and oxygen-driven penalty in side reactions.

Combined with the schematic overview in Figure **??**, this figure provides a visual justification of why the lamellar spacing is the key variable rather than an alloy with the same phases in a different configuration. Pure Al represents a combination

of surface passivation, non-uniform dissolution, gas evolution, and irregular redeposition. Lamellar alloy separates these roles for an active aluminum and conductive intermetallic guide. The selected route provides no variations in chemistry but varies the microstructure length scale. Therefore, this design creates an experimental challenge: the same eutectic phase pair produces different electrochemical results if the spacing changes the trade-off between access length and oxygen-sensitive cathodic area.

2. Sample Series and Oxygen-Controlled Testing

Lamellar spacing is chosen as the independent variable because solidification theory provides a direct way of changing the lamellar period for a given phase pair without altering the Al-Cu composition. According to the Jackson-Hunt analysis and further studies of eutectic growth, the square of the spacing depends on the growth conditions, while the phase diagram indicates that the Al-Cu composition is good for creating a two-phase lamellar architecture rather than isolated islands [34–39]. The series covers spacing of 180, 280, 420, 650, and 1100 nm. This range includes an over-refined case, an intermediate candidate, the established 420 nm spacing comparator, and two coarse cases. Pure Al and monolithic Al_2Cu samples are also considered as controls.

Table 1: Spacing library and intended electrochemical role.

Electrode	λ (nm)	Interface density (μm^{-1})	Al width (nm)	Al_2Cu width (nm)	Role in the comparison
E-$Al_{82}Cu_{18}$-180	180	11.1	64	116	Very high junction density with strong oxygen-sensitive cathodic area.
E-$Al_{82}Cu_{18}$-280	280	7.1	100	180	Balanced access length and continuous intermetallic guidance.
E-$Al_{82}Cu_{18}$-420	420	4.8	150	270	Established 420 nm morphology with low-oxygen reversibility.
E-$Al_{82}Cu_{18}$-650	650	3.1	232	418	Coarse channels with increased passivation-limited transport length.
E-$Al_{82}Cu_{18}$-1100	1100	1.8	393	707	Long Al domains with high probability of nonuniform stripping.

The literature on Al–Cu alloy corrosion confirms the relevance of the proposed separation in geometry. Cu-containing intermetallic phases in aluminum alloys may function as local cathodes in some circumstances and promote the dissolution of neighboring regions of Al, yet these same intermetallics may serve as an interconnected cathode current redistribution network and change surface reactions in another configuration [29–33]. Thus, the distributed particle network and periodic lamellar structure are different in their electrochemical behavior. In the design proposed here, the Al/Al_2Cu interface density is used not just as an indicator of the alloy's corrosion potential but also as a multi-task descriptor that may facilitate the accessibility of aluminum and provide additional area for cathodic reactions depending on oxygen concentration.

The series of spacing values in Table 1 transforms the structural idea into numerical values. When the lamellar period is 180 nm, each Al region is very thin (only 64 nm) and located close to Al_2Cu, and when the lamellar period is 1100 nm, the width of the Al region reaches 393 nm, and the majority of aluminum has passivating properties similar to bulk Al. The choice of 280 nm spacing value is significant because it provides an increase of the interface density by 48% compared to the reference 420 nm value while avoiding too high a density of interfaces characteristic of the 180 nm value. Thus, it is a possible oxygen-tolerant solution before obtaining any data from full cells.

The measurement procedure in Table 2 eliminates the following pitfall in alloy-anode comparisons: a material cannot be accepted just because it has good performance in some particular environment. The anode should demonstrate low polarization and impedance, acceptable oxygen tolerance, stable surface evolution, and effective cathode utilization in a constant electrolyte and cathode. Thus, the proposed procedure does not allow using only one descriptor as an explanation. Lamellar period is the selection variable, but the conclusions require consistency between all outputs.

Table 2: Measurements linking anode spacing with cell output.

Measurement group	Variables retained	Reason for inclusion
Microstructure	Period, Al width, Al_2Cu width, interface density	Separates length scale from alloy chemistry.
Oxygen stress	0.13, 1.5, 5.0, and 13.6 mg L^{-1} dissolved oxygen	Tests whether the low-polarization candidate survives imperfect deaeration.
Symmetric cells	Overpotential, R_{ct}, energy efficiency, stable operation time	Measures anode reversibility before cathode limitations enter.
Surface response	Selective stripping, guided plating, roughness, failure regime	Connects voltage stability to physical morphology.
Full cells	Rate capacity, specific energy, long-cycle retention	Determines whether the anode gain produces usable cathode output.

These levels of oxygen were chosen to provide four distinctly different practical operating conditions. The level of 0.13 mg L^{-1} is representative of careful deaeration and provides the low oxygen control. The levels of 1.5 mg L^{-1} and 5.0 mg

L^{-1} represent oxygen infiltration or partial purging such that the electrolyte is unsaturated, but cathodic reactions may affect the voltage response. Finally, 13.6 mg L^{-1} represents an oxygen-rich stress state which emphasizes leakage sensitivity and demonstrates whether the microstructure remains durable when cathodic reactions are promoted. This range is critical because the same anode can be satisfactory in the low oxygen case and fail the durability criterion in the less ideal electrolyte.

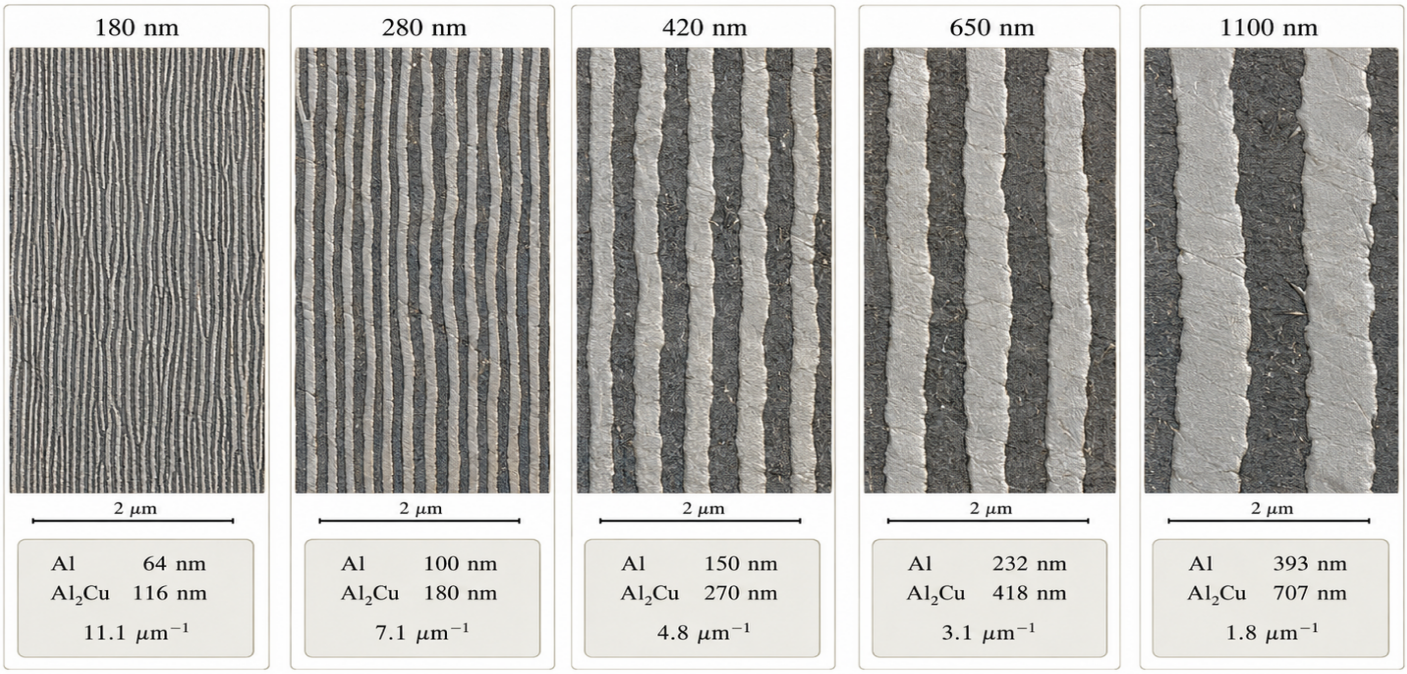

Figure 2: Measured Al–Cu lamellar spacing series.

There are also controls which are essential to interpretation. Pure Al provides a test of active aluminum in the absence of periodic intermetallic guidance, while monolithic Al_2Cu provides a test of the conductive and noble phase in the absence of an available Al matrix. Poor performance relative to lamellar eutectics proves that the desired response cannot come from either material individually. The controls ensure that the 280 nm optimum is not the result of mere presence of the copper or accessibility of the aluminum, but comes instead from proper domain size.

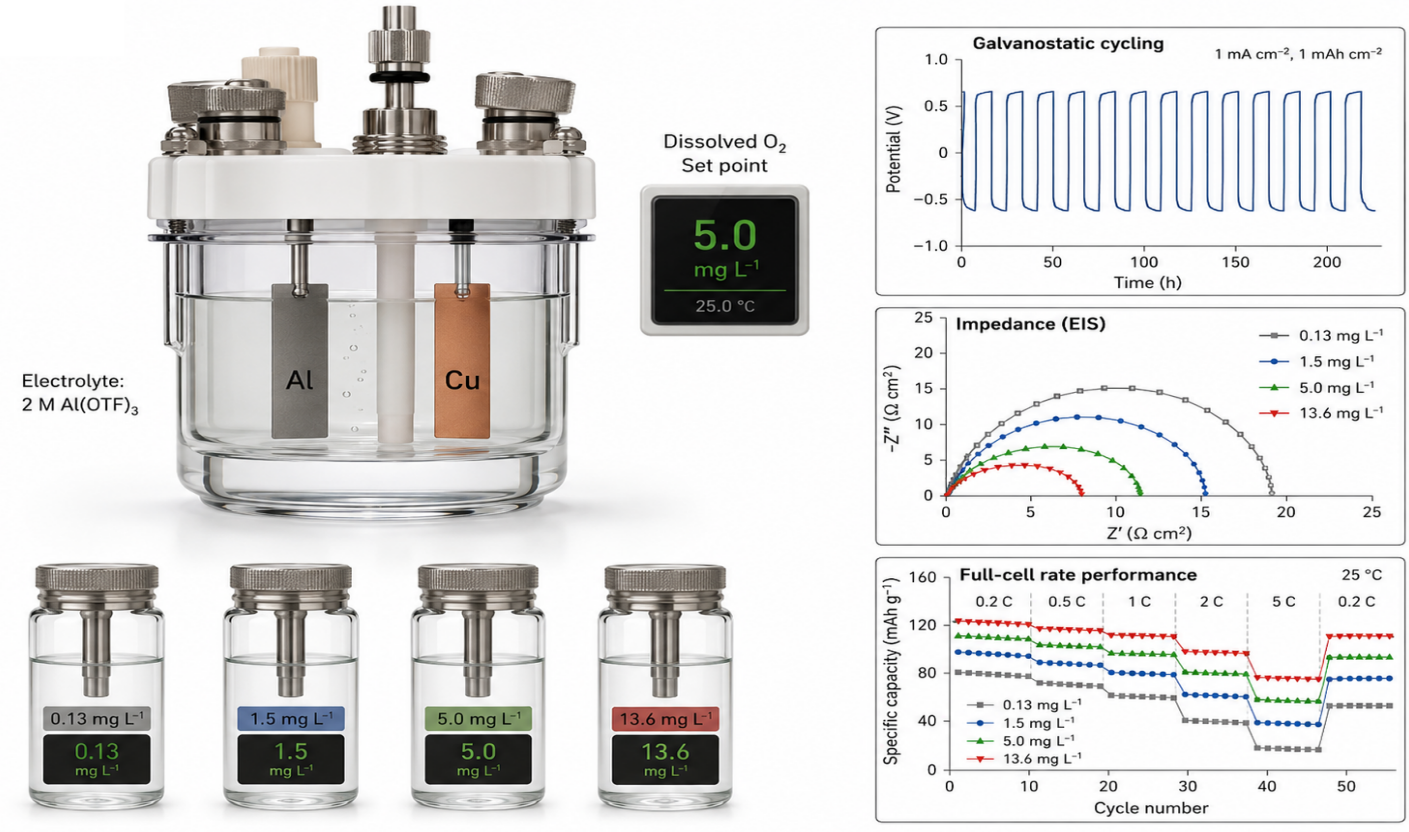

Figure 3: Oxygen-controlled electrochemical testing.

The five periods are divided into a direct 420 nm comparator and four controlled departures from ideal spacing. Tests at

180 and 280 nm determine whether refining increases Al access, while tests at 650 and 1100 nm show whether coarsening decreases oxygen sensitive cathodic surface area at the expense of passivation length. This scheme ties each electrochemical response to a specific Al width, Al_2Cu width, interface density, and oxygen content rather than just alloy designation.

Figure 2 represents the procedure for transforming the microstructure into an electrochemical variable. The processes of melting, directional solidification, cutting, polishing, and rapid transition are fixed to prevent possible errors arising from improper surface preparation. The interface density curve represents the inverse geometric trend, whereas the width curve indicates the physical transport lengths that are faced by the anode. One important thing to note is that the finest and the coarsest samples cannot be deemed better based on the geometric analysis alone. The finest sample guarantees maximum accessibility but is prone to excessive cathodic area, while the coarsest sample has minimum cathodic area but is vulnerable to passivation of Al channels.

Figure 3 represents the setup and output windows, which indicate the way in which oxygen is used as a controlled electrochemical stressor. The dissolved oxygen levels are linked with the same aqueous electrolyte, electrode geometry, and temperature. In this way, overpotential, impedance, and cell output can be analyzed as reactions to oxygen exposure and lamellar period.

3. Oxygen-Resolved Spacing Criterion

In the form of the spacing criterion, the relationship describes the tradeoff between the galvanic advantage of access and oxygen-enhanced degradation. In the case of a lamellar period λ, the density of the Al/Al_2Cu interfaces per length unit is proportional to $2/\lambda$. The modification of this geometric factor by penalties for an excess of refinement and oxygen is given by the following expression:

$$\Phi(\lambda, C_{O_2}) = \left(\frac{\lambda_0}{\lambda}\right) \exp\left[-\left(\frac{\lambda_{\min}}{\lambda}\right)^2\right] \left[1 + \beta \log\left(1 + \frac{C_{O_2}}{C_0}\right)\right]^{-1}. \tag{1}$$

Here, $\lambda_0 = 420$ nm determines the comparator interval; $\lambda_{\min} = 110$ nm protects against unregulated bias towards excessive fineness of spacing; and $C_0 = 0.13$ mg L^{-1} is highly deaerated electrolyte. The parameter of Φ is not a general corrosion constant but rather a measure of spacing which compels the comparison to recognize that the same intermetallic structure may direct aluminum precipitation and promote parasitic reductions.

The kinetic parameters are described by three equations:

$$\eta_{0.5} = \eta_{\min} + A(\Phi - \Phi^*)^2 + B \log\left(1 + \frac{C_{O_2}}{C_0}\right), \tag{2}$$

$$R_{ct} = R_{\min} + \frac{K}{\Phi + \epsilon} + R_{ox} \log\left(1 + \frac{C_{O_2}}{C_0}\right), \tag{3}$$

$$k_{fade} = k_0 + k_{coarse}\left(\frac{\lambda}{\lambda_0}\right)^{1.3} + k_{fine}\left(\frac{\lambda_{\min}}{\lambda}\right)^2 + k_{O_2}\frac{C_{O_2}}{C_{O_2} + C_0}. \tag{4}$$

The formulas separate three penalties, which are difficult to differentiate using only a voltage trace: one related to the move from the optimal galvanic accessibility, a contribution of charge transfer resistance in terms of the oxide affected interface and a fade coefficient increasing in both microstructural extremes. Such procedure is based on the electrochemical kinetics and impedance analysis principle, in which polarization, charge transfer and transport (diffusion) limitations have to be discriminated before the mechanism can be established [40–44].

The spacing criterion is used as the numerical interpretation of the same physical criterion. Period of lamellar structure, width of aluminum regions, Al2Cu width and interface density are structural inputs that can be measured, while the oxygen contribution does not allow choosing the most advanced sample by the amount of interfaces present in it. Therefore, the relevant range is expected to arise where the guidance provided by intermetallic phase is intact, but the amount of the cathodic region accessible to the oxygen dissolved in electrolyte is sufficient.

The oxygen penalty is represented by the formula

$$\Omega_O(\lambda) = \frac{\eta(\lambda, 13.6) - \eta(\lambda, 0.13)}{\log(13.6/0.13)}. \tag{5}$$

The importance of this property arises from the fact that aqueous fuel cells can seldom be run continuously in a completely oxygen-free environment. An electrode with low polarization only when thoroughly purged of oxygen in the electrolyte solution is not as advantageous as an electrode that suffers a little from oxygen leak. The criteria for electrode choice include

$$S = 0.35\eta_{0.5}^{-1} + 0.25R_{ct}^{-1} + 0.20T_{stable}^{*} + 0.20\Omega_O^{-1}, \tag{6}$$

where T_{stable}^{*} is the normalized stable stripping/plating duration. The score does not eliminate the requirement for repeat measurements. It ensures that no candidate can be chosen unless it exhibits low polarization, low R_{ct}, stable stripping/plating, and low oxygen sensitivity.

The asymmetry of Eq. 1 is intentional. It favors reduced spacing via the λ_0/λ factor, since close guidance of intermetallics favors electron removal and reduces the distance over which the Al can remain active beneath an oxide-modified surface. It punishes over-refinement by means of the exponential factor, as it takes into account the possibility that very dense noble

sites accelerate cathodic reactions. The oxygen term decreases the descriptor in the case of increased dissolved oxygen content, so as to punish candidates that are attractive only in oxygen-free electrolyte with an overly optimistic score. The formula is sufficiently simple for lab testing, yet maintains the core chemical struggle of the anode.

The R_{ct} descriptor of Eq. 3 supplies a second check. An increase in R_{ct} alongside reduced overpotential would suggest that the lowering of the kinetic barrier for stripping and plating due to the presence of intermetallic network does not occur. The decrease of overpotential and R_{ct} at 280 nm simultaneously are important precisely for that reason. It shows that the anode is not just more reactive but also more electrochemically reversible under identical electrolyte conditions.

The fade descriptor of Eq. 4 prevents a candidate from being considered based on its initial overpotential value alone. Coarse lamellae are penalized since large Al domains may passivate and dissolve inhomogeneously upon repeated cycles. Very fine lamellae are penalized since interfacial area becomes a catalyst for side-reactions. Oxygen stress brings one more non-linearity since reduction of water, reduction of oxygen, pH changes in the interface and oxide repairs can all interact with each other during prolonged cycling. The expression highlights the aging mechanisms that have to be studied in order to confirm the spacing claim: coarse-channel passivation, fine-spacing cathodic reactivity, oxygen reduction, water reduction and oxide repair.

4. Results and Discussion

The symmetric-cell results confirm the first step in the spacing response. Pure Al is not a good negative electrode control for the overpotential (U), charge transfer resistance (R_{ct}), energy efficiency (η) and stable stripping and plating times being 1750 mV, 3880Ω, 71.5% and less than 30 h correspondingly. Monolithic Al_2Cu demonstrates the same good efficiency in the last three parameters, having $U = 300$ mV, $R_{ct} = 455\Omega$ but still cannot provide the necessary prolonged reversible aluminum reservoir. Among the eutectic samples, E-$Al_{82}Cu_{18}$-280 provides the best low oxygen performance with $U = 38$ mV, $R_{ct} = 112\Omega$, $\eta = 99.6\%$ and the longest stable time 3000 h. 420 nm reference provides high stability and low polarization, having 53 mV, 160 Ω, 99.4% and 2000 h respectively. Increasing of the reference period to 650 and 1100 nm leads to higher polarization and lower stability.

Table 3: Low-oxygen symmetric-cell performance.

Electrode	λ (nm)	$\eta_{0.5}$ (mV)	R_{ct} (Ω)	Energy efficiency (%)	Stable stripping/plating (h)
Pure Al	–	1750	3880	71.5	< 30
Al_2Cu	–	300	455	94.2	180
E-$Al_{82}Cu_{18}$-180	180	42	120	99.5	2600
E-$Al_{82}Cu_{18}$-280	280	38	112	99.6	3000
E-$Al_{82}Cu_{18}$-420	420	53	160	99.4	2000
E-$Al_{82}Cu_{18}$-650	650	67	205	98.8	1500
E-$Al_{82}Cu_{18}$-1100	1100	96	305	97.4	800

The values presented in Table 3 confirm that the lamellar structure is the key parameter of the material. In case if the copper-containing chemistry was the crucial one, monolithic Al_2Cu should show the eutectic-type characteristics; however, it still remains quite polarized and non-stable material. In case if the interface density was the crucial one, 180 nm period should be the dominant one, whereas the 280 nm sample provides the lowest polarization and resistance. It means that 280 nm period provides the optimal positioning of Al regions close to the conductive Al-Cu guide areas while keeping enough spacing to reduce cathodic reaction areas.

Electrode	Overpotential (mV)	Charge-transfer resistance (Ω)	Energy efficiency (%)	Stable time (h)
Pure Al	1750 mV	3880 Ω	71.5%	<30 h
Al_2Cu	300 mV	455 Ω	94.2%	180 h
E-AlCu-180 (180 nm)	42 mV	120 Ω	99.5%	2600 h
E-AlCu-280 (280 nm)	**38 mV**	**112 Ω**	**99.6%**	**3000 h**
E-AlCu-420 (420 nm)	53 mV	160 Ω	99.4%	2000 h
E-AlCu-650 (650 nm)	67 mV	205 Ω	98.8%	1500 h
E-AlCu-1100 (1100 nm)	96 mV	305 Ω	97.4%	800 h

Figure 4: Low-oxygen symmetric-cell reversibility.

The comparison of the results shown in Figure 4 confirms the robustness of the symmetric-cell conclusion. Pure-Al and monolithic Al_2Cu controls still remain far from the eutectic group, while the 280 nm sample combines the lowest overpotential, lowest R_{ct}, highest energy efficiency and longest stable operation. The stable time parameter is particularly important because it eliminates the possibility of any initial activation effect. E-$Al_{82}Cu_{18}$-280 is not just easier to activate in the beginning of the test; it provides the delay in the interfacial damage accumulation for thousands of hours. Compared to E-$Al_{82}Cu_{18}$-420 sample, it reduces overpotential approximately 28%, R_{ct} about 30% and increases the stable time for 50%.

The extent of the pure-Al penalty is informative in itself. A 1750 mV overpotential at the same nominal current density indicates that almost all the useful voltage of the battery is dissipated by the negative electrode prior to evaluating the cathode. Similarly, the high value of 3880 Ω is not merely an inconvenient kinetic obstacle but the indication of a blocking interface and a metastable reaction layer. The monolith Al_2Cu test proves that high conductivity and nobility are not sufficient conditions to overcome this difficulty. It provides a lower kinetic impedance in comparison with pure Al but is still lacking alternating activity and guide layers necessary for continuous aluminum transport.

The kinetic hierarchy is explicitly illustrated by the resistance shell in Figure 5. The outermost ring made from pure aluminum illustrates the blocking effect of the hydrated oxide film, and monolithic Al_2Cu lies outside of the eutectic combination due to the absence of the distributed active aluminum reservoir. The sample of 280 nm has the smallest resistance and overpotential value simultaneously, thus proving that the optimum period is chosen according to the simultaneous minimum of both interfacial resistance and polarization.

The difference between 180 and 280 nm periods is minimal, but the scientific significance is great. Both periods are much more effective than 420 nm in terms of low oxygen pressure, and both illustrate that further refinement of the structure from 420 nm is effective. However, the 280 nm period provides the minimum resistance and maximum stability time. It proves that the most refined morphology is not necessarily the most stable one. It can be concluded that the surface formed by 180 nm period contains too many active junctions as well as electron accepting places for oxygen and water.

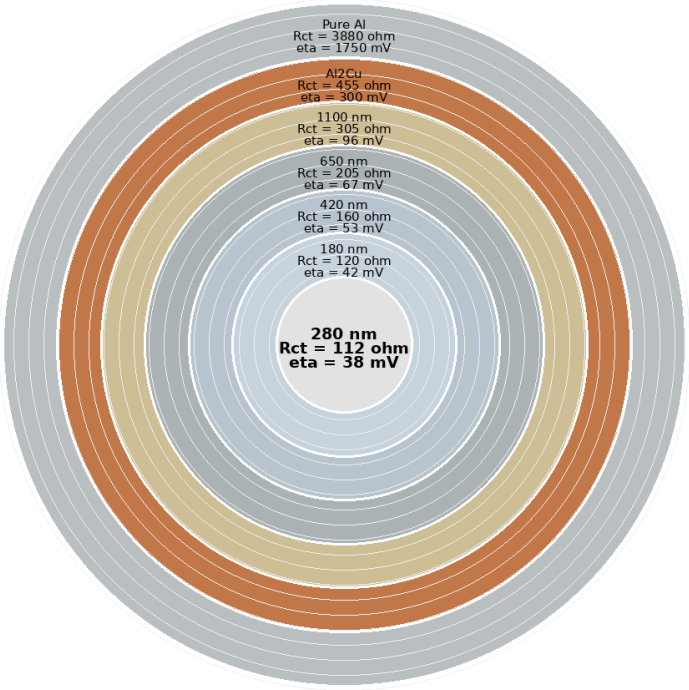

Sample	280 nm	180 nm	420 nm	650 nm	1100 nm	Al2Cu	Pure Al
Rct (ohm)	112	120	160	205	305	455	3880
Overpotential (mV)	38	42	53	67	96	300	1750

Figure 5: Spacing-dependent resistance and overpotential.

The presence of dissolved oxygen leads to reinterpreting the ordering of alloys as a robustness ordering to environment. For 0.13 mg L^{-1} of oxygen content, the 180 and 280 nm electrodes have similar levels of overpotential, namely 42 and 38 mV correspondingly. With 13.6 mg L^{-1} of oxygen, the difference in the overpotentials grows to 96 versus 78 mV. Thus, the advantages of finer structure decrease as oxygen concentration grows. The overpotential of the 420 nm reference increases from 53 to 112 mV, whereas the coarse 650 and 1100 nm electrodes grow to 146 and 218 mV correspondingly. It means that both extremes are sensitive to oxygen content due to two distinct mechanisms: fine lamellae have too much cathodic intermetallic interfaces, and coarse lamellae form passivated Al domains, which cannot be reactivated homogeneously.

The surface oxygen penalty shown in Figure 6 provides the most significant evidence for the choice of 280 nm electrode among the other fine-spaced candidates. Every specimen shows increasing polarization due to oxygen growth; however, the height of the terrace grows fastest in the case of coarse specimens, whereas 280 nm specimens have the smallest penalty

terrace. In the case of 180 nm specimens, the initial position is near the 280 nm electrode but loses the advantage in the case of rich oxygen content. Thus, oxygen reduction and local alkalinization become more important for noble intermetallic surfaces with increasing noble intermetallic area, whereas passivation occurs in case of large Al regions. The best anode has the minimal oxygen-normalized penalty.

Table 4: Oxygen-dependent overpotential values.

Electrode	$\eta_{0.13}$ (mV)	$\eta_{1.5}$ (mV)	$\eta_{5.0}$ (mV)	$\eta_{13.6}$ (mV)	Mechanistic reading
E-$Al_{82}Cu_{18}$-180	42	53	72	96	Strong low-oxygen activation but excessive cathodic area at high oxygen.
E-$Al_{82}Cu_{18}$-280	38	46	59	78	Lowest oxygen-normalized penalty and best overall spacing.
E-$Al_{82}Cu_{18}$-420	53	65	84	112	Reliable reference morphology but less competitive after spacing refinement.
E-$Al_{82}Cu_{18}$-650	67	84	110	146	Coarse Al domains increase passivation-limited polarization.
E-$Al_{82}Cu_{18}$-1100	96	122	160	218	Long transport paths dominate the oxygen-stress response.

The data in Table 4 provide the most precise answer to the oxygen part of the research question. The E-$Al_{82}Cu_{18}$-280 electrode remains preferred for every oxygen content, not only for the case of 0.13 mg L^{-1} dissolved oxygen. The increase of the overpotential from 38 to 78 mV for oxygen variation is lower compared to the same normalized variations for other candidates. It is mechanically plausible due to the fact that 280 nm spacing has enough intermetallic continuity to ensure charge distribution but does not have excessive cathodic intermetallic interfaces as over-refined 180 nm specimen does.

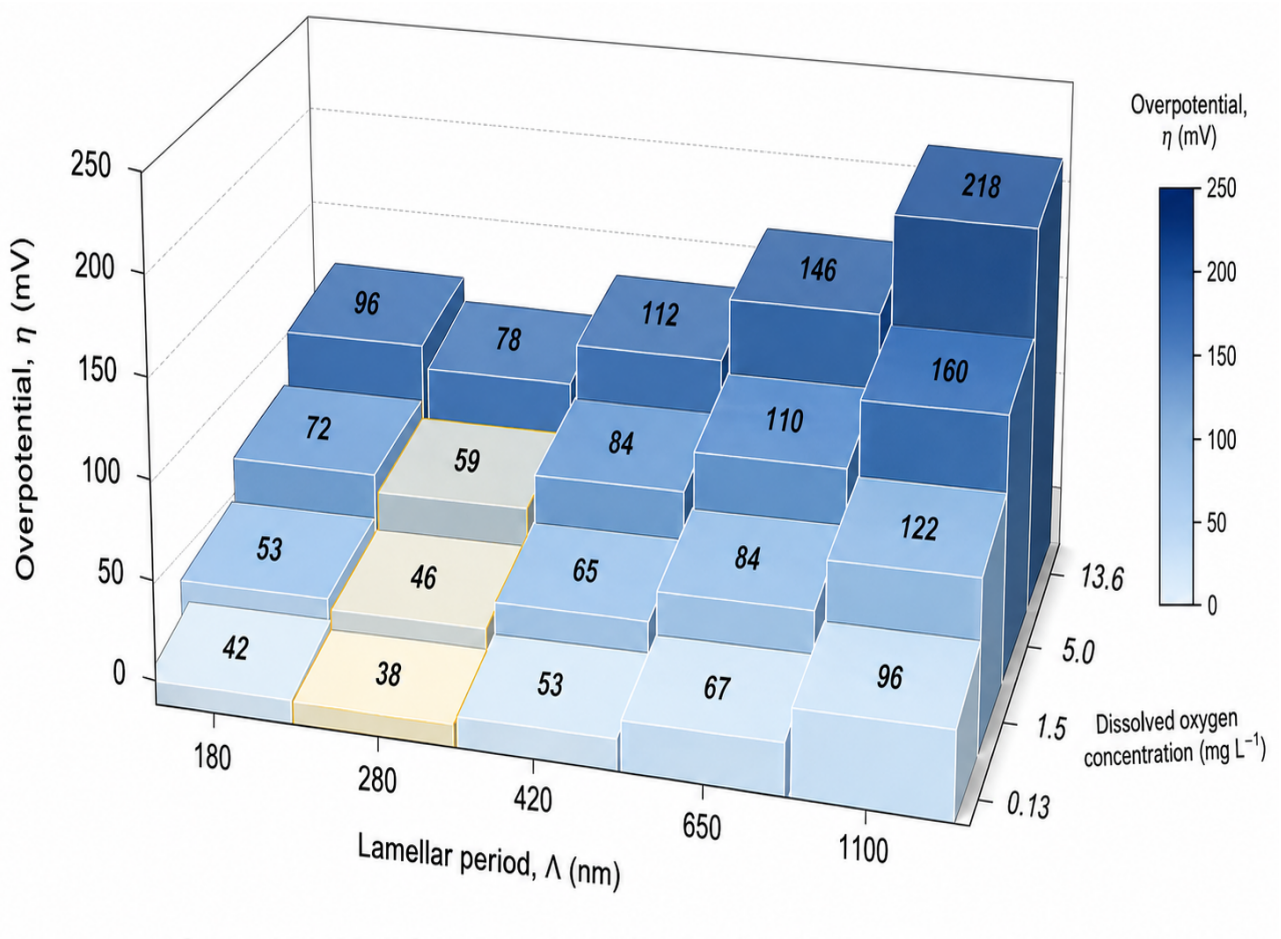

Figure 6: Dissolved-oxygen penalty by lamellar period.

The dependence on oxygen distinguishes another two notions of stability. There can be materials which have stable voltage profile in deoxygenated state but unstable when their voltage profile is dependent on oxygen. In case of aqueous cells, the latter notion of stability is usually more crucial since maintaining oxygen-free atmosphere during manufacturing of material, packaging, electrolyte soaking, and operation itself is complicated. The 280 nm spacing was chosen since it meets both requirements, that is, has the lowest low-oxygen overpotential and the highest resistance to oxygen-related penalty.

Based on the rough results, lower cathodic area alone does not have to be the goal. Under the assumption of oxygen reduction being the only limiting factor, the surfaces with 650 and 1100 nm periods could be expected to show better performance under oxygen stress due to having fewer interfaces per unit length. Instead, their polarization is even larger for all oxygen levels. Therefore, it is clear that transport limited by passivation of aluminum takes precedence once Al channels become too wide. Such behavior corresponds to a surface where oxide affected areas are too distant from the conductive intermetallics to get periodically reactivated during stripping and plating.

Surface evolution represents another test for the ranking based on the voltage curves. Namely, Al stripping should not involve breaking up the surface into islands, while plating should not involve redepositing into protrusions. Such lamellar network structure is possible only if the Al_2Cu ribs stay contiguous and close enough to the active Al regions. The wider

spacings lead to local passivation within the Al channels, while the narrower spacings aggravate parasitic reactions at the abundant junction networks.

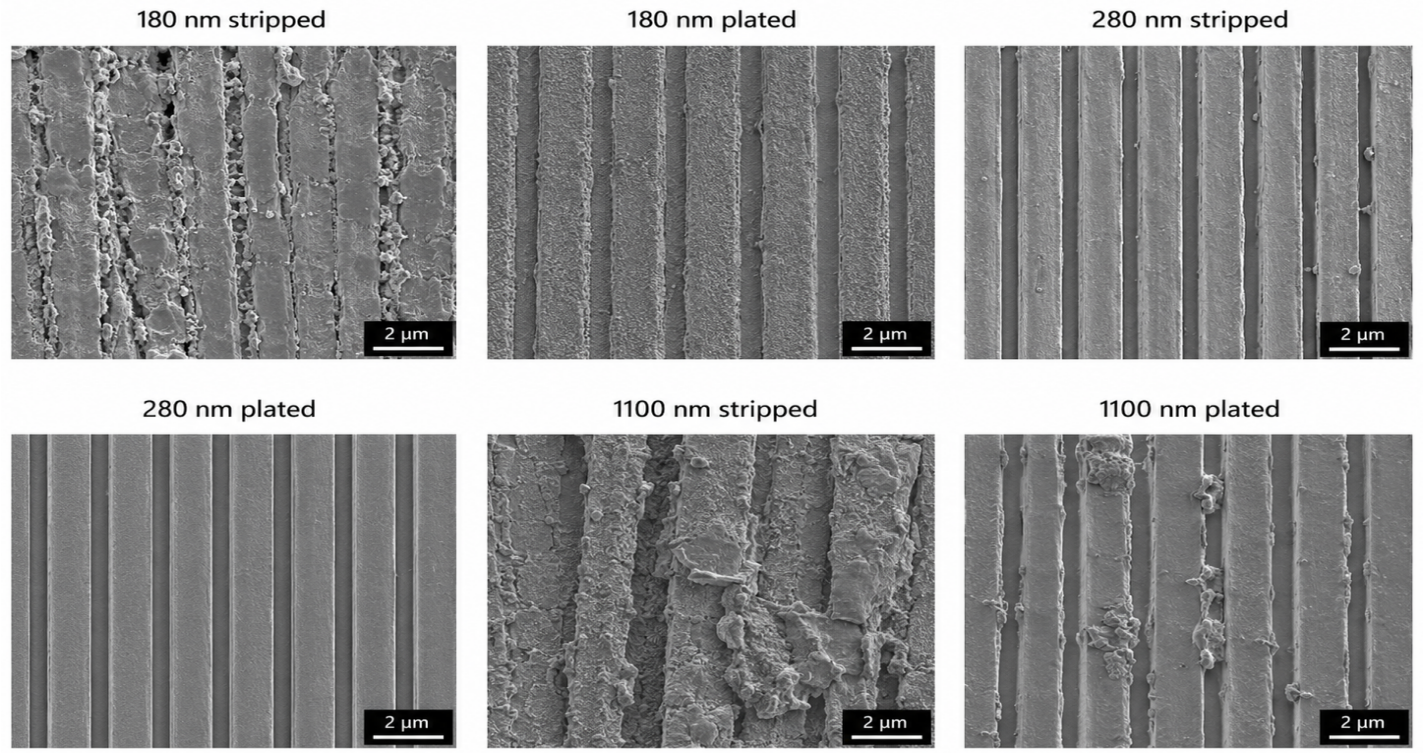

Figure 7: Surface morphology after stripping and plating.

The panels of Figure 7 correlate the findings of electrochemistry with the morphology of surfaces. In particular, the selective Al dissolution is not necessarily undesirable provided that the intermetallic skeleton continues to spread the current. The guided redeposition should happen instead, because this ensures that newly formed Al gets back into the channels. Post-cycling results show that pure Al undergoes severe roughening, the 420 nm eutectic has some improvement but is not optimized yet, while 280 nm surface retains the channel structure the best. Thus, the failure map confirms the validity of the above explanation: 180 nm surface is limited by cathodic activity enhanced by oxygen reduction, while 650 and 1100 nm surfaces are limited by transport and passivation.

The analysis of surface is consistent with the impedance measurements. The post-cycling roughness makes the interface heterogeneous, and the fitted charge-transfer resistance could reflect multiple mechanisms such as oxide diffusion, exposed metal dissolution, gas coverage, and variations in electrolyte composition. In contrast, the morphology retaining the lamellar channels reduces the uncertainty and makes it clear what charge transfer process is responsible for the observed low resistance. This explains why the result of the surface measurement supports the electrochemical ranking: the low R_{ct} is achieved due to preservation of the reaction architecture rather than random corrosion that temporarily lowers the resistance.

Noticeably, this equation is a charge compensation representation. Hydrated MnO could incorporate many aspects of atomic interactions: the insertion of the aluminum ions, protons, hydration shell restructuring, and structural relaxation of the oxide lattice. Reduction of the anode hysteresis thus improves the cathodic capacity of the cell [7, 27, 28].

The theory helps understand why dendrite inhibition in aqueous aluminum batteries should not be analogized with that of lithium metal. This is because aluminum electrodeposition happens simultaneously with oxidation, hydrolysis, and hydrogen generation. As a result, protrusive growth of the Al dendrites is just one among many possible reasons for cell failure. In this case, the layered structure of the Al–Cu network works as a distribution scaffolding rather than as a soft matrix. The effectiveness of such a structure is based on its ability to preserve conductivity after removal of the Al layer and re-deposition of the same material in the initial locations.

Translation into the full cell is crucial because otherwise there is no point in considering an anode, since it will only affect the performance of the entire device. The cathode remains unchanged as $\mathrm{Al}_x\mathrm{MnO}_2 \cdot n\mathrm{H}_2\mathrm{O}$, and the electrolyte composition as 2 M $\mathrm{Al(OTF)}_3$ solution with 0.2 M $\mathrm{Mn(OTF)}_2$. Cathode reaction can be written as

$$\mathrm{Al}_x\mathrm{MnO}_2 \cdot n\mathrm{H}_2\mathrm{O} + 3(y-x)e^- + (y-x)\mathrm{Al}^{3+} \rightleftharpoons \mathrm{Al}_y\mathrm{MnO}_2 \cdot n\mathrm{H}_2\mathrm{O}. \tag{7}$$

In the analysis shown in Fig. 8, all other factors including cathode, separator, electrolyte and the construction of the cell have been kept fixed in order for the performance difference to be attributed to the anode. While the Al-metal shows the loss of most of the cathode capacity at high rate conditions, E-$\mathrm{Al}_{82}\mathrm{Cu}_{18}$-420 restores the majority of the lost capacity through minimizing the anode polarization. E-$\mathrm{Al}_{82}\mathrm{Cu}_{18}$-280 has the best capability of transferring the symmetric-cell capacity into the full cell.

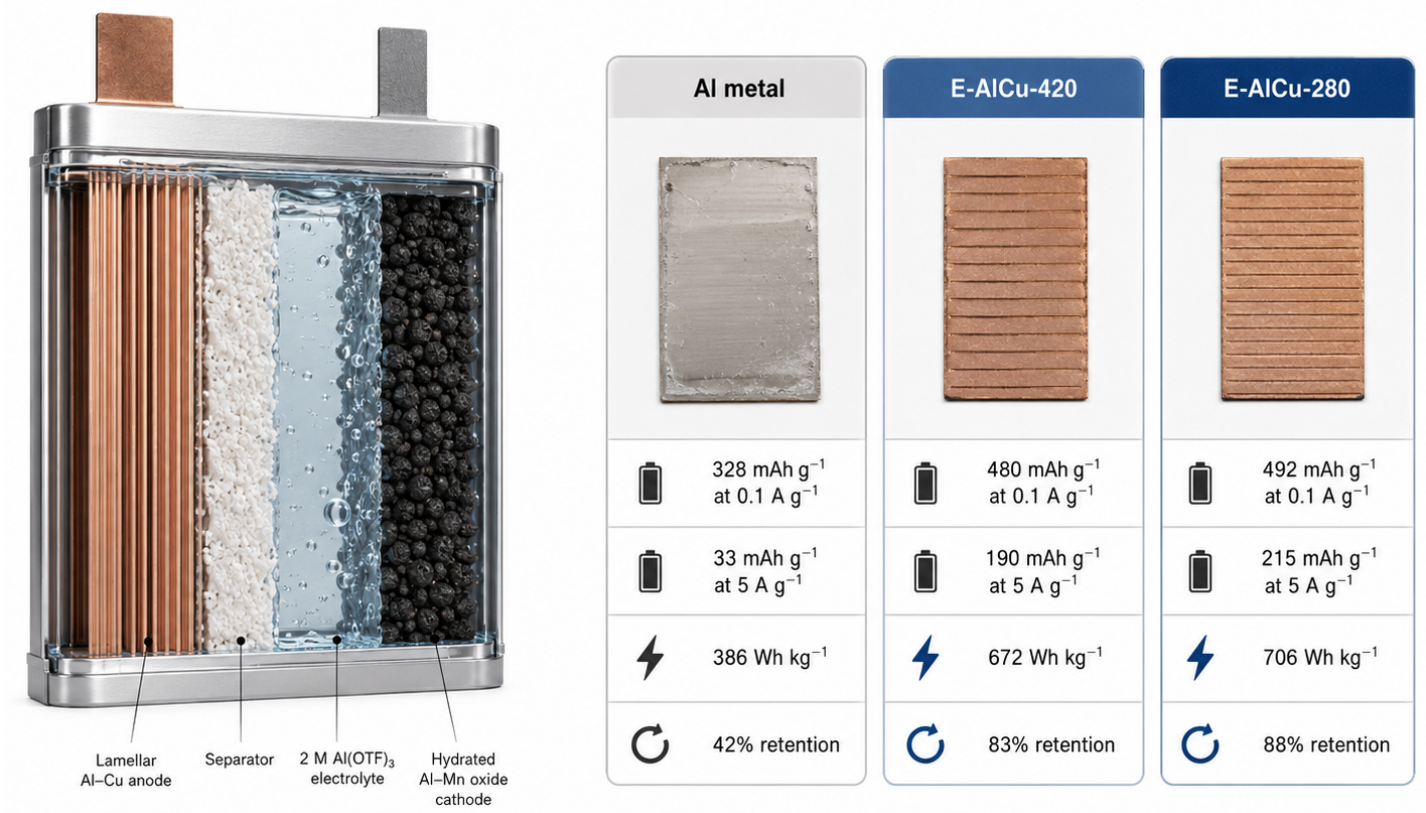

Figure 8: Full-cell output with the hydrated Al–Mn oxide cathode.

The full cell values provided in Table 5 clarify why even slight anode-polarization improvement is important. The transition from the 420 nm anode to the 280 nm anode results in increase of 0.1 A g^{-1} capacity from 480 to 492 mAh g^{-1} and 5 A g^{-1} capacity from 190 to 215 mAh g^{-1}. The specific energy improves from 672 to 706 Wh kg^{-1} and the retention window widens from 83% for 400 cycles to 88% for 600 cycles. The performance of pure-Al battery is poor despite the high theoretical capacity of aluminum, thus proving the assumption that the issue is related to reversible interfacial utilization rather than insufficient aluminum.

Table 5: Full-cell output with fixed $Al_xMnO_2 \cdot nH_2O$ cathode.

Anode	$\eta_{0.5}$ (mV)	R_{ct} (Ω)	$Q_{0.1}$ (mAh g^{-1})	Q_5 (mAh g^{-1})	Energy at 0.1 A g^{-1} (Wh kg^{-1})	Retention
Al metal	1750	3880	328	33	386	42% at 80 cycles
E-$Al_{82}Cu_{18}$-420	53	160	480	190	672	83% at 400 cycles
E-$Al_{82}Cu_{18}$-280	38	112	492	215	706	88% at 600 cycles

The improvement in the full cell performance is especially noticeable under high-rate conditions. At 0.1 A g^{-1} current, the difference in capacity between 480 and 492 mAh g^{-1} looks insignificant, as the cathode has enough time to access its capacity with the use of 420 nm anode. However, at 5 A g^{-1}, the capacity increases from 190 to 215 mAh g^{-1}. The low impedance of the anode allows maintaining the cathode capacity under high-rate conditions. It is logical that the hydrated manganese oxide exhibits such behavior since the multi-valence charge-compensation process depends on transport, solvation, and local structure. Reduction of the negative electrode capacity does not change the cathode chemistry but only allows approaching the intrinsic capabilities of the cathode.

Long-cycle retention provides the second full-cell test. The pure-Al cell rapidly loses capacity, as the anode consumes voltage and active material through passivation, roughening, and parasitic reaction. The 420 nm eutectic prevents these losses, but the 280 nm morphology both retains more capacity and cycles longer. As expected by the symmetric-cell result, the anode hierarchy transfers between cell types. A material that appears good in symmetric cells but fails in full-cell retention cannot solve the research problem. The 280 nm material is good at both steps.

A synthesis ties the various tests together into a selection criterion. Useful design space is not the whole eutectic range of Al-Cu alloys. Instead, it is the range where intermetallic network is continuous enough for guiding currents but not so dense that reduction of oxygen dominates the cathode reaction. Therefore, the identified score interval corresponds to a physical regime where length of Al access, continuity of Al_2Cu, oxygen sensitivity, impedance, and cathode voltage utilization are all acceptable.

This synthesis shown in Figure 9 delivers the solution as a spacing map. The fine-spacing region is discarded due to cathodic excess being oxygen-sensitive. The coarse-spacing region is rejected since passivation length and uneven current density are dominant there. Thus, the highlighted 240–330 nm region combines 38 mV low-oxygen overpotential, 112 Ω R_{ct}, 40 mV penalty from oxygen within the measured range, and 3000 h stable symmetric cycling performance. Consequently, the E-$Al_{82}Cu_{18}$-280 is a material target, not just experimental result.

The optimal 280 nm spacing value does not mean that all Al–Cu alloys will perform well in water, that all copper-rich phases should be used, or that electrolyte engineering is not necessary. Interfacial modification, concentrated electrolyte, hydrated eutectic electrolyte, and additives are still key methods for achieving stability of aluminum-water interface [45–49]. The presented values prove that in case of the eutectic $Al_{82}Cu_{18}$ phase pair, lamellar period should be considered as an oxygen-dependent optimization parameter, rather than a passive microstructural attribute. Future electrolytes or interphases might change the optimum, but they will need to be optimized with the same combined criteria of access length, cathode area, oxygen response, impedance, and full-cell performance.

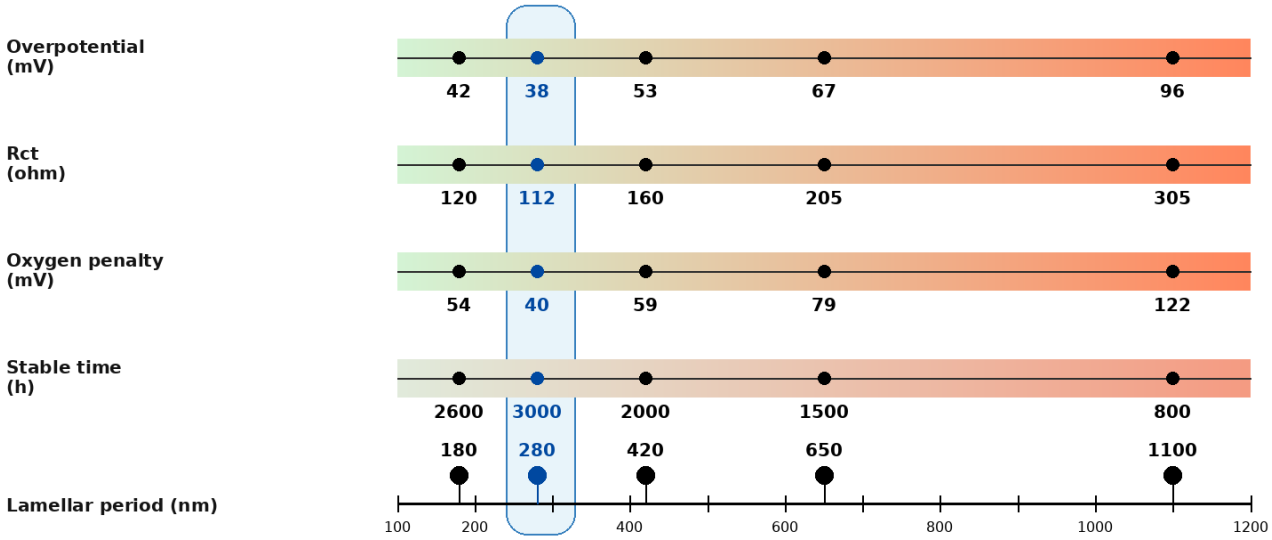

Figure 9: Oxygen-tolerant spacing window.

Moreover, the selection rule suggests a practical experimental scheme that goes beyond five periods measured in this work. Any lab can produce the series of specimens with specific spacing, measure period and phase continuity, discard specimens with discontinuous or irregular lamellae, and apply the oxygen-resolved symmetric-cell test to identify the region where the oxygen penalty is minimal. Then, full cells will be used to verify best candidates, since cathode cycling is much slower and resource-intensive. The experimental sequence follows the causal chain in direct way: microstructure screening, oxygen-resolved testing, and finally full cells validation.

The restriction of the selection rule is its dependence on the particular electrolyte, cathode, and phase pair used here. Transition to chloride, perchlorate, hydrate-melt, or deep eutectic electrolyte would change the oxygen term by altering the water activity, solvation effect, film chemistry, and corrosion potential. New cathode can modify the voltage window and affect the importance of anode loss. However, these restrictions do not undermine the main result; they define its scope. The result is the microstructure criterion for eutectic $Al_{82}Cu_{18}$ alloy in aqueous aluminum-manganese system, not a universal constant for all aluminum batteries.

5. Experiment and Analysis

Eutectic $Al_{82}Cu_{18}$ ingots were made from high-purity aluminum and copper by arc melting in argon atmosphere with subsequent remeltings to enhance chemical homogeneity. Lamellar period of 180, 280, 420, 650, and 1100 nm was reached with the help of directional solidification or controlled cooling procedure. In the 420-nm morphology there are approximate Al and Al_2Cu widths of 150 and 270 nm. The each ingot is cut perpendicular to lamellae and then grinded with 7000 mesh abrasive paper followed by cleaning in deoxygenated ultrapure water and ethanol and drying under inert gas. Next, the ingot pieces are rapidly transferred into inertial chamber before assembling cells. For control samples made from pure Al and monolithic Al_2Cu, the dimensions and grinding history are identical to those of the alloy sample.

The $Al_xMnO_2 \cdot nH_2O$ cathode material was synthesized hydrothermally at 150 °C for 24 h with stirring from 20 mM $KMnO_4$, 20 mM NH_4Cl, and 5 mM $Al(NO_3)_3$. Next, the obtained product was washed and dried and mixed with Super P carbon and poly(vinylidene difluoride) in 70:20:10 mass ratio. The resulting slurry was coated on stainless-steel foil with active material loading of 1.0 mg cm^{-2}. The cathode materials and dimensions, separator, electrolyte, and voltage window are always kept the same in the full cell comparison so that capacity changes could be attributed only to the anode material.

Phase identification was accomplished by X-ray diffraction using Cu Kα radiation. Lamellar microstructure was investigated by optical microscopy, scanning electron microscopy, energy-dispersive X-ray spectroscopy, and transmission electron microscopy. The lamellar period and phases widths were measured from at least 50 line profiles of each sample and interface density was calculated from the measured repeat distance. The surface chemistry before and after cycling was studied by X-ray photoelectron spectroscopy and Raman spectroscopy, focusing on species of aluminum oxide/hydroxides, Cu-rich intermetallic exposure, and corrosion products generated by oxygen stress. The dissolved oxygen content was measured with oxygen probe calibrated right before injection of electrolyte into the cell.

The symmetric cells were assembled from identical electrodes separated with glass fiber membrane and filled with 0.25 mL of 2 M aqueous $Al(OTF)_3$. The concentration of dissolved oxygen was regulated with nitrogen or oxygen purging to 0.13,

1.5, 5.0, or 13.6 mg L^{-1}. The stripping and plating tests were carried out at 0.5–2.5 mA cm^{-2}. Electrochemical impedance spectra from 100 kHz to 10 mHz were recorded with 10 mV perturbation and fitted with equivalent circuit with internal resistance, charge-transfer resistance, constant phase element, and Warburg impedance. Hydrogen evolution was registered by gas chromatography or inline pressure sensor to separate beneficial activation from cathodic acceleration.

The full cells were fabricated from an anode made from Al-Cu alloy, cathode from $Al_xMnO_2 \cdot nH_2O$, glass fiber separator, and aqueous 2 M $Al(OTF)_3$ electrolyte with 0.2 M $Mn(OTF)_2$. Galvanostatic experiments were performed in the voltage range 0.5-1.8 V. The capacity and specific energy were determined from the mass of cathode active material. Long term cycling was performed at 0.5 A g^{-1} after three formation cycles at 0.1 A g^{-1}. The ranking is valid only if the same anode is still better in terms of symmetric-cell low-oxygen performance, oxygen-stress response, surface stability, and full-cell output.

Replicate treatment is based on the same hierarchy. Morphological measurements are repeated from several line profiles to avoid assignment of nominal period from one favorable image. Electrochemical data are analyzed in terms of both average values and failure criteria like voltage spikes, sudden impedance growth, gas production, or visible surface degradation. Sample producing low overpotentials but demonstrating instability repeatedly cannot be considered a promising candidate. It is especially true for pure aluminum since each local event can dominate in voltage profile and for very fine lamellae because parasitic reactions can occur slowly.

Table 6: Validation workflow without chemistry changes.

Validation phase	Required evidence
Microstructure confirmation	Reproducible lamellar period, continuous Al/Al_2Cu arrangement, and phase purity by XRD and microscopy.
Deaerated reversibility	Low $\eta_{0.5}$, low R_{ct}, high energy efficiency, and stable stripping/plating in deaerated electrolyte.
Oxygen robustness	Limited overpotential increase across 0.13–13.6 mg L^{-1} dissolved oxygen with controlled gas-evolution evidence.
Surface durability	Channel-preserved stripping/plating and absence of severe roughening or isolated active islands after cycling.
Full-cell transfer	Improved rate capacity, specific energy, and long-cycle retention with the same $Al_xMnO_2 \cdot nH_2O$ cathode and electrolyte.

Table 6 presents the validation steps, which enable replicability without introducing any additional parameters. The anode cannot be said to have achieved optimization unless all these aspects of the microstructure, symmetric cell, oxygen tolerance, post-cycling morphologies, and full cell have yielded the same spacing. This helps to ensure that the selection of the material does not depend on just one favorable number.

6. Conclusion

The key question posed was whether lamellar Al–Cu anodes for aqueous aluminum–manganese batteries must be chosen using an oxygen threshold condition alone or an oxygen-normalized spacing that predicts full-cell performance. The answer is that oxygen-normalized spacing is necessary. Low interface density can help up until when the cathodic intermetallic area becomes excessive because of the dissolved oxygen content. Excessive refinement leads to the opposite type of failure, in that it enhances the length of Al access and passivation-polarization problems. The optimal spacing is hence intermediate rather than small.

The quantitative analysis reveals E-$Al_{82}Cu_{18}$-280 to be the most promising choice among the five-period spacing series. Compared to the 420 nm reference sample, the reduction to 280 nm period results in overpotential drop from 53 to 38 mV, R_{ct} drop from 160 to 112 Ω, stability of symmetric cell increased from 2000 to 3000 hours, and minimum penalty from oxygen over the range of 0.13–13.6 mg L^{-1} dissolved oxygen content. In the fixed $Al_xMnO_2 \cdot nH_2O$ full cell, the same anode brings about increase in rate capacity from 190 to 215 mAh g^{-1} at 5 A g^{-1}, increase in specific energy from 672 to 706 Wh kg^{-1}, and 88% capacity after 600 cycles. Such improvements solve the research problem since the anode selected via oxygen-threshold metric is the one that improves cell utilization.

The design guideline is precise: eutectic aluminum–copper anodes for aqueous batteries must be fabricated within an oxygen-resistant lamellar period of approximately 240–330 nm. Such length scale allows to retain sufficient aluminum/cuprate contact to guide electrochemical reactions without the oxygen-enhanced secondary reactions. This rule is also verifiable in experiments. Future work should synthesize the full-spacing series, quantitatively measure oxygen consumption and hydrogen evolution at the same current density, and find out whether additives to electrolyte or artificial interphase move the optimum without breaking the balance between galvanic access and secondary reactions' area.

The more general lesson is that microstructure-controlled alloy anodes must always be characterized with environmental metadata. The lamellar period, phase fraction, polishing history, dissolved oxygen, electrolyte volume, and time between polishing and assembly may influence the appearance of aluminum reversibility. Absence of such details may cause two nominally identical Al–Cu samples to seem inconsistent despite following the same physics. Selection according to oxygen-threshold spacing is not just a design guideline but a reporting recommendation as well: in an aqueous aluminum anode study, the alloy microstructure and oxygen state used in tests must be reported.

Conflict of Interest

The author declares no competing interests.

References

[1] J.-M. Tarascon and M. Armand, "Issues and challenges facing rechargeable lithium batteries," *Nature*, **414**, 359–367 (2001).

[2] B. Dunn, H. Kamath and J.-M. Tarascon, "Electrical energy storage for the grid: A battery of choices," *Science*, **334**, 928–935 (2011).

[3] M. Armand and J.-M. Tarascon, "Building better batteries," *Nature*, **451**, 652–657 (2008).

[4] J. B. Goodenough and K.-S. Park, "The Li-ion rechargeable battery: A perspective," *Journal of the American Chemical Society*, **135**, 1167–1176 (2013).

[5] N. Nitta, F. Wu, J. T. Lee and G. Yushin, "Li-ion battery materials: Present and future," *Materials Today*, **18**, 252–264 (2015).

[6] E. Faegh, B. Ng, D. Hayman and W. E. Mustain, "Practical assessment of the performance of aluminium battery technologies," *Nature Energy*, **6**, 21–29 (2021).

[7] Q. Ran, H. Shi, H. Meng, S. Cheng, Q. Cai, H. Han, C. He, K. Wang, J. Li, B. Wei, Y. Long, T. Liao, Z. Tang and L. Mai, "Aluminum-copper alloy anode materials for high-energy aqueous aluminum batteries," *Nature Communications*, **13**, 576 (2022).

[8] M. Pourbaix, *Atlas of Electrochemical Equilibria in Aqueous Solutions*, 2nd ed., National Association of Corrosion Engineers, Houston (1974).

[9] J. R. Galvele, "Transport processes and the mechanism of pitting of metals," *Journal of the Electrochemical Society*, **123**, 464–474 (1976).

[10] G. S. Frankel, "Pitting corrosion of metals: A review of the critical factors," *Journal of the Electrochemical Society*, **145**, 2186–2198 (1998).

[11] Z. Szklarska-Smialowska, "Pitting corrosion of aluminum," *Corrosion Science*, **41**, 1743–1767 (1999).

[12] E. McCafferty, *Introduction to Corrosion Science*, Springer, New York (2010).

[13] M.-C. Lin, M. Gong, B. Lu, Y. Wu, D.-Y. Wang, M. Guan, M. Angell, C. Chen, J. Yang, B.-J. Hwang and H. Dai, "An ultrafast rechargeable aluminium-ion battery," *Nature*, **520**, 324–328 (2015).

[14] G. A. Elia, K. Marquardt, K. Hoeppner, S. Fantini, R. Lin, E. Knipping, W. Peters, J.-F. Drillet, S. Passerini and R. Hahn, "An overview and future perspectives of aluminum batteries," *Advanced Materials*, **28**, 7564–7579 (2016).

[15] F. Ambroz, T. J. Macdonald, T. Nann and A. B. Jorge Sobrido, "Evaluation of strategies for rechargeable aluminium batteries," *Advanced Energy Materials*, **7**, 1602093 (2017).

[16] D. Yuan, J. Zhao, W. Manalastas Jr., S. Kumar and M. Srinivasan, "Emerging rechargeable aqueous aluminum ion battery: Status, challenges, and outlooks," *Nano Materials Science*, **2**, 248–263 (2020).

[17] B. E. Jia, A. Q. Thang, C. Yan, C. Liu, C. Lv, Q. Zhu, J. Xu, J. Chen, H. Pan and Q. Yan, "Rechargeable aqueous aluminum-ion battery: Progress and outlook," *Small*, **18**, 2107773 (2022).

[18] X. Zheng, C. Han, C. S. Lee, W. Yao, C. Zhi and Y. Tang, "Materials challenges for aluminum ion based aqueous energy storage devices: Progress and prospects," *Progress in Materials Science*, **143**, 101253 (2024).

[19] L. Li, S. Jia, Y. Shi, C. Wang, H. Qiu, Y. Ji, M. Cao and D. Zhang, "Recent progress in aluminum anodes for high-performance rechargeable aqueous Al-ion batteries," *Inorganic Chemistry Frontiers*, **11**, 2246–2259 (2024).

[20] X. Wang, J. Li, Y. Zhang and H. Zhou, "Progress on aqueous rechargeable aluminium metal batteries," *Industrial Chemistry & Materials*, article D4IM00031E (2025).

[21] R. Mori, "Aqueous rechargeable aluminum battery: A mini review," *Energy Advances*, **4**, 1321–1336 (2025).

[22] H. Yu, Y. Zhang, X. Liu, Z. Chen, W. Li, J. Wang, Y. Tang, C. Zhi and co-workers, "Activation and stabilization strategies of aluminum metal anode toward high performance aqueous Al metal batteries," *Advanced Materials*, 2507164 (2025).

[23] S. Liu, J. J. Hu, N. F. Yan, G. L. Pan, G. R. Li and X. P. Gao, "Aluminum storage behavior of anatase TiO_2 nanotube arrays in aqueous solution for aluminum ion batteries," *Energy & Environmental Science*, **5**, 9743–9746 (2012).

[24] Z. Li, K. Xiang, W. Xing, W. C. Carter and Y.-M. Chiang, "Reversible aluminum-ion intercalation in Prussian blue analogs and demonstration of a high-power aluminum-ion asymmetric capacitor," *Advanced Energy Materials*, **5**, 1401410 (2015).

[25] S. Liu, G. L. Pan, G. R. Li and X. P. Gao, "Copper hexacyanoferrate nanoparticles as cathode material for aqueous Al-ion batteries," *Journal of Materials Chemistry A*, **3**, 959–962 (2015).

[26] T. Koketsu, J. Ma, B. J. Morgan, M. Body, C. Legein, W. Dachraoui, M. Giannini, A. Demortiere, M. Salanne, F. Dambournet and others, "Reversible magnesium and aluminium ions insertion in cation-deficient anatase TiO_2," *Nature Materials*, **16**, 1142–1148 (2017).

[27] S. He, J. Wang, X. Zhang, J. Chen, Z. Wang, T. Yang, Z. Liu, Y. Liang, B. Wang, S. Liu and H. Yu, "A high-energy aqueous aluminum-manganese battery," *Advanced Functional Materials*, **29**, 1905228 (2019).

[28] C. Wu, S. Gu, Q. Zhang, Y. Bai, M. Li, Y. Yuan, H. Wang, X. Liu, Y. Yuan, N. Zhu, F. Wu, H. Li, L. Gu and J. Lu, "Electrochemically activated spinel manganese oxide for rechargeable aqueous aluminum battery," *Nature Communications*, **10**, 73 (2019).

[29] B. Mazurkiewicz and A. Piotrowski, "The electrochemical behaviour of the Al_2Cu intermetallic compound," *Corrosion Science*, **23**, 697–707 (1983).

[30] R. G. Buchheit, "A compilation of corrosion potentials reported for intermetallic phases in aluminum alloys," *Journal of the Electrochemical Society*, **142**, 3994–3996 (1995).

[31] N. Birbilis and R. G. Buchheit, "Electrochemical characteristics of intermetallic phases in aluminum alloys: An experimental survey and discussion," *Journal of the Electrochemical Society*, **152**, B140–B151 (2005).

[32] J. Li and J. Dang, "A summary of corrosion properties of Al-rich solid solution and secondary phase particles in Al alloys," *Metals*, **7**, 84 (2017).

[33] H. Zhou, W. Yao, C. Du, S. Song and R. Wu, "Corrosion behavior of the Al_2Cu intermetallic compound and coupled Al_2Cu/Al," *International Journal of Electrochemical Science*, **12**, 9542–9554 (2017).

[34] K. A. Jackson and J. D. Hunt, "Lamellar and rod eutectic growth," *Transactions of the Metallurgical Society of AIME*, **236**, 1129–1142 (1966).

[35] R. Trivedi, P. Magnin and W. Kurz, "Theory of eutectic growth under rapid solidification conditions," *Acta Metallurgica*, **35**, 971–980 (1987).

[36] W. Kurz and D. J. Fisher, *Fundamentals of Solidification*, 4th ed., Trans Tech Publications, Switzerland (1998).

[37] J. L. Murray, "The aluminium-copper system," *International Metals Reviews*, **30**, 211–234 (1985).

[38] D. A. Porter, K. E. Easterling and M. Y. Sherif, *Phase Transformations in Metals and Alloys*, 3rd ed., CRC Press, Boca Raton (2009).

[39] O. Zobac, A. Kroupa, A. Zemanova and K. W. Richter, "Experimental description of the Al-Cu binary phase diagram," *Metallurgical and Materials Transactions A*, **50**, 3805–3815 (2019).

[40] A. J. Bard and L. R. Faulkner, *Electrochemical Methods: Fundamentals and Applications*, 2nd ed., Wiley, New York (2001).

[41] J. Newman and K. E. Thomas-Alyea, *Electrochemical Systems*, 3rd ed., Wiley-Interscience, Hoboken (2004).

[42] D. D. Macdonald, "Reflections on the history of electrochemical impedance spectroscopy," *Electrochimica Acta*, **51**, 1376–1388 (2006).

[43] M. E. Orazem and B. Tribollet, *Electrochemical Impedance Spectroscopy*, Wiley, Hoboken (2008).

[44] A. Lasia, *Electrochemical Impedance Spectroscopy and its Applications*, Springer, New York (2014).

[45] Q. Zhao, M. J. Zachman, W. I. Al Sadat, J. Zheng, L. F. Kourkoutis and L. A. Archer, "Solid electrolyte interphases for high-energy aqueous aluminum electrochemical cells," *Science Advances*, **4**, eaau8131 (2018).

[46] A. Ejigu, P. A. Greatorex-Davies, D. A. Walsh and R. A. W. Dryfe, "Optimization of electrolytes for high-performance aqueous aluminum-ion batteries," *Journal of Power Sources*, **520**, 230818 (2022).

[47] P. Meng, Y. Dong, L. Zhou, L. Mai and co-workers, "Air-stable binary hydrated eutectic electrolytes with unique solvation structures for aqueous aluminum batteries," *Advanced Energy Materials*, **13**, 2300949 (2023).

[48] Q. Sun, Y. Pang, X. Li, H. Zhang and J. Liu, "Constructing an artificial SEI layer rich in AlF_3 based on molecular scale in aqueous aluminum batteries to avoid anode passivation and hydrogen evolution reactions," *Chemical Engineering Journal*, **489**, 151296 (2024).

[49] M. R. Raj, K. Zaghib and G. Lee, "Advanced aqueous electrolytes for aluminum-ion batteries: Challenges and opportunities," *Energy Storage Materials*, **78**, 104211 (2025).